Received: 7 October 2022 | Accepted: 21 December 2022

DOI: 10.1002/pamm.202200118

Hydraulically induced fracturing in heterogeneous porous media using a TPM-phase-field model and geostatistics

Arndt Wagner[1,3,*], **Alixa Sonntag**[1], **Sebastian Reuschen**[2], **Wolfgang Nowak**[2,3], and **Wolfgang Ehlers**[1,3]

[1] Institute of Applied Mechanics (CE), University of Stuttgart, 70569 Stuttgart, Germany
[2] Institute for Modelling Hydraulic and Environmental Systems, University of Stuttgart, 70569 Stuttgart, Germany
[3] Stuttgart Center for Simulation Science (SC SimTech), University of Stuttgart, 70569 Stuttgart, Germany

Hydraulically induced fracturing is widely used in practice for several exploitation techniques. The chosen macroscopic model combines a phase-field approach to fractures with the Theory of Porous Media (TPM) to describe dynamic hydraulic fracturing processes in fully-saturated porous materials. In this regard, the solid's state of damage shows a diffuse transition zone between the broken and unbroken domain. Rocks or soils in grown nature are generally inhomogeneous with material imperfections on the microscale, such that modelling homogeneous porous material may oversimplify the behaviour of the solid and fluid phases in the fracturing process. Therefore, material imperfections and inhomogeneities in the porous structure are considered through the definition of location-dependent material parameters. In this contribution, a deterministic approach to account for predefined imperfection areas as well as statistical fields of geomechanical properties is proposed. Representative numerical simulations show the impact of solid skeleton heterogeneities in porous media on the fracturing characteristics, e. g. the crack path.

1 Introduction

Hydraulic fracturing is a versatile and important procedure for a broad variety of geophysical applications applied in saturated and unsaturated porous materials. Examples are exploitation techniques, enhanced oil and gas recovery or the estimation of in-situ stresses. The coupled processes occurring during fluid-driven fracturing processes in porous media are not fully understood yet and the application of hydraulic fracturing remains empirical. A basic difficulty is that the direct observation of propagating fractures enveloped in the underground is difficult. Therefore, modelling and simulation techniques provide a good option for gaining insight into the fracturing process. There are different methods to describe both the strongly coupled behaviour of porous media with pore content and the fracturing process. A comprehensive view on the continuum-mechanical description of porous media can be found for the Biot theory [1] or poro-elasticity [2], mixture-based approaches [3] or [4], and the Theory of Porous Media (TPM) [5] just to name a few. In particular, the TPM allows for a rigorous and consistent formulation and is therefore chosen here. Considering the fracturing process in porous media, the phase-field approach has gained more and more attention in recent years [6], [7] or [8]. Hereby, a scalar order parameter describes the solid's state of damage with a diffuse transition zone between the intact and broken domain. This approach avoids the occurrence of a discontinuous jump in the fracturing process and, thus, facilitates the numerical implementation. An embedded phase-field approach within the TPM enables furthermore a transfer from Darcy-type flow in the intact porous material to Stokes-type flow in the fully broken area in a consistent manner. This is particularly important to mimic the changing flow regime after the crack opened, as shown for fully saturated porous material in [9] or [10] and for partially saturated porous material in [11]. Natural porous materials are generally heterogeneous with material imperfections on the microscale. Therefore, modelling homogeneous porous material may oversimplify the behaviour of the fracturing process. In this contribution, material imperfections and inhomogeneities in the porous structure are included through the definition of location-dependent material parameters. Thereby, predefined imperfection areas are considered as well as statistical fields of geomechanical properties. The main focus in this contribution is to discuss the impact of heterogeneities in porous media on the fracturing characteristics, e. g. crack evolution and crack path.

2 Modelling approach

As an excerpt from previous works on fracturing processes in fully saturated porous media [10] and [12], the basic TPM-phase-field model is briefly introduced in this chapter. Following a virtual homogenisation (volumetrical averaging), the microscopic structure of the real pore morphology is smeared out and leads to a macroscopic model of superimposed and interacting continua. The overall aggregate φ is composed of a materially incompressible solid skeleton φ^S and a materially incompressible pore liquid φ^L, viz.:

$$\varphi = \bigcup_{\alpha} \varphi^{\alpha} = \varphi^S \cup \varphi^L \quad \text{with} \quad \alpha = \{S, L\}. \tag{1}$$

* Corresponding author: e-mail arndt.wagner@mechbau.uni-stuttgart.de, phone +49 711 685 66375, fax +49 711 685 66347

As basic quantities to express the volumetric composition of the porous media, volume fractions are classically defined via $n^\alpha := \mathrm{d}v^\alpha/\mathrm{d}v$ with $n^S + n^L = 1$, where the sum of the volume fractions equals always one, i. e. the so-called saturation condition. Furthermore, two different density functions are introduced, the realistic (effective) density $\rho^{\alpha R} := \mathrm{d}m^\alpha/\mathrm{d}v^\alpha$ and the partial density $\rho^\alpha := \mathrm{d}m^\alpha/\mathrm{d}v$. Since the local mass element $\mathrm{d}m^\alpha$ is related in the latter case to the bulk volume element $\mathrm{d}v$ of the so-called representative elementary volume (REV), the partial density can be interpreted as a volumetrically averaged density on the macroscale, which is also seen by the relation $\rho^\alpha = n^\alpha \rho^{\alpha R}$. In an isothermal environment, the specific balance equations of immiscible constituents are given by the mass and momentum balances, viz.:

$$(\rho^\alpha)'_\alpha + \rho^\alpha \operatorname{div} \mathbf{x}'_\alpha = 0 \qquad \text{and} \qquad \rho^\alpha \mathbf{x}''_\alpha = \operatorname{div} \mathbf{T}^\alpha + \rho^\alpha \mathbf{g} + \hat{\mathbf{p}}^\alpha . \tag{2}$$

Therein, $\hat{\mathbf{p}}^\alpha$ is the direct momentum production term of constituent φ^α, $\mathbf{T}^\alpha$ defines the Cauchy stresses of φ^α, and $\mathbf{g}$ is the gravitation vector. To ensure that the constitutive equations for the stresses and the production terms are thermodynamically admissible, they have to fulfil the entropy inequality. Moreover, the Helmholtz free energy ψ^α of each constituent φ^α is stated to depend only on constitutive variables of the individual component under consideration (principle of phase separation), namely $\psi^S = \psi^S(\mathbf{F}_S)$ and $\psi^L = \psi^L(-)$. The standard constitutive choice of ψ^S depending on the deformation gradient $\mathbf{F}_S$ or, equivalently, on the Green-Lagrangean strain $\mathbf{E}_S$ for fully saturated porous media is extended for the consideration of fracturing processes therein. The basic concept to embed a phase-field approach within the TPM induces to include a phase-field variable

$$\phi^S(\mathbf{x}, t) \in [0, 1] \quad \text{with} \begin{cases} \phi^S = 0 & : \text{intact solid phase,} \\ 0 < \phi^S < 1 & : \text{diffuse interface,} \\ \phi^S = 1 & : \text{fully broken solid phase,} \end{cases} \tag{3}$$

and its solid-material gradient $\operatorname{Grad}_S \phi^S$ into the set of dependencies via $\psi^S = \psi^S(\mathbf{E}_S, \phi^S, \operatorname{Grad}_S \phi^S)$. In this regard, we further restrict to a small-strain approach of the porous solid, where $\mathbf{E}_S \approx \boldsymbol{\varepsilon}_S$ and $\operatorname{Grad}_S(\,\cdot\,) \approx \operatorname{grad}(\,\cdot\,)$. After some modifications [10], the evaluation of non-dissipative terms of the entropy inequality using a Coleman-Noll procedure yields the constitutive restrictions

$$\boldsymbol{\sigma}^S_E = \rho^S_0 \frac{\partial \psi^S}{\partial \boldsymbol{\varepsilon}_S} \qquad \text{and} \qquad \operatorname{div}\left((\phi^S)'_S \, \rho^S_0 \, \frac{\partial \psi^S}{\partial \operatorname{grad} \phi^S} \right) = 0 . \tag{4}$$

Therein, $\boldsymbol{\sigma}^S_E$ is the linearised solid extra stress related via the linearised solid strains $\boldsymbol{\varepsilon}_S$ to the solid deformation field $\mathbf{u}_S$. Taking advantage of proportionality properties, the dissipation inequality is satisfied by the relations

$$\begin{aligned} (\phi^S)'_S &= -\frac{1}{M}\left[\rho^S_0 \frac{\partial \psi^S}{\partial \phi^S} - \operatorname{div}\left(\rho^S_0 \frac{\partial \psi^S}{\partial \operatorname{grad} \phi^S} \right) \right] , \\ \mathbf{T}^L_E &= 2\,(\phi^S)^2\, n^L \mu^{LR}\, \mathbf{D}_L \qquad \text{and} \qquad \hat{\mathbf{p}}^L_E = -(1-\phi^S)^2 \frac{(n^L)^2 \mu^{LR}}{K^S}\, \mathbf{w}_L . \end{aligned} \tag{5}$$

Thus, a thermodynamical restriction for the evolution equation of ϕ^S is obtained, where $M > 0$ denotes the mobility parameter. Obviously, the evolution of ϕ^S only depends on the energetic changes of the porous solid and is a direct result of the solid deformation, which can be indirectly induced via a fluid pressure during hydraulic fracturing conditions. The viscous extra stress $\mathbf{T}^L_E$ includes the effective dynamic viscosity μ^{LR} of the pore liquid and the phase-field parameter ϕ^S such that the liquid extra stress $\mathbf{T}^L_E$ can be neglected in the intact porous domain but occur in the fractured zone. In accordance, the extra momentum production $\hat{\mathbf{p}}^L_E$ depends, besides the viscosity μ^{LR} and the intrinsic permeability K^S, on the phase-field parameter ϕ^S and, thus, vanishes in the fully fractured zone but dominates the pore-fluid flow in the unbroken domain. Following basic papers on phase-field fracture [13] and [14], the solid Helmholtz free energy is postulated as

$$\rho^S_0 \psi^S(\boldsymbol{\varepsilon}_S, \phi^S, \operatorname{grad} \phi^S) = \left[(1-\phi^S)^2 + \eta^S_r \right] \rho^S_0 \, \psi^{S+}(\boldsymbol{\varepsilon}^+_S) + \rho^S_0 \, \psi^{S-}(\boldsymbol{\varepsilon}^-_S) + G_c \, \Gamma^S(\phi^S, \operatorname{grad} \phi^S) . \tag{6}$$

In (6), contributions from the tensile and compression energy and the fracture energy are combined. As described in [13], a spectral decomposition of the symmetric strain tensor $\boldsymbol{\varepsilon}_S = \sum_i \lambda_{Si}\, \mathbf{n}_{Si} \otimes \mathbf{n}_{Si}$ in terms of eigenvalues λ_{Si} and their eigenvectors $\mathbf{n}_{Si}$ allows for a split of $\boldsymbol{\varepsilon}_S = \boldsymbol{\varepsilon}^+_S + \boldsymbol{\varepsilon}^-_S$, yielding

$$\begin{aligned} \rho^S_0 \, \psi^{S+}(\boldsymbol{\varepsilon}^+_S) &= \mu^S \, (\boldsymbol{\varepsilon}^+_S \cdot \boldsymbol{\varepsilon}^+_S) + \tfrac{1}{2} \lambda^S \left\{ \tfrac{1}{2} (\operatorname{tr} \boldsymbol{\varepsilon}_S + |\operatorname{tr} \boldsymbol{\varepsilon}_S|) \right\}^2 , \quad \text{with} \quad \boldsymbol{\varepsilon}^+_S = \sum\nolimits_i \frac{\lambda_{Si} + |\lambda_{Si}|}{2}\, \mathbf{n}_{Si} \otimes \mathbf{n}_{Si} , \\ \rho^S_0 \, \psi^{S-}(\boldsymbol{\varepsilon}^-_S) &= \mu^S \, (\boldsymbol{\varepsilon}^-_S \cdot \boldsymbol{\varepsilon}^-_S) + \tfrac{1}{2} \lambda^S \left\{ \tfrac{1}{2} (\operatorname{tr} \boldsymbol{\varepsilon}_S - |\operatorname{tr} \boldsymbol{\varepsilon}_S|) \right\}^2 , \quad \text{with} \quad \boldsymbol{\varepsilon}^-_S = \sum\nolimits_i \frac{\lambda_{Si} - |\lambda_{Si}|}{2}\, \mathbf{n}_{Si} \otimes \mathbf{n}_{Si} , \end{aligned} \tag{7}$$

where $\boldsymbol{\varepsilon}^+_S$ only contains positive and $\boldsymbol{\varepsilon}^-_S$ only negative eigenvalues. Furthermore, μ^S and λ^S are the Lamé constants. Moreover, a residual stiffness η^S_r is postulated for the tensile energy in (6) to prevent zero stiffness for a fully damaged state. The fracture

energy in (6) includes the critical energy release rate (crack resistance) G_c of brittle fracture and the fracture surface density function $\Gamma^S(\phi^S, \operatorname{grad}\phi^S) = (\phi^S)^2/2\epsilon + \frac{1}{2}\epsilon \operatorname{grad}\phi^S \cdot \operatorname{grad}\phi^S$. Therein, the internal length-scale parameter ϵ smears out a diffuse interface in the damaged zone, where $0 < \phi^S < 1$. Since ϵ regulates the width of the transition zone, a discrete (sharp) crack is recovered for $\epsilon \to 0$. A detailed discussion of this topic is reported in [10] and [12]. The introduced energy (6) allows for the evaluation of the restrictions claimed by the entropy inequality, i. e. the evolution equation of ϕ^S is found as

$$(\phi^S)'_S \;=\; \frac{1}{M}\left[2(1-\phi^S)\,\rho_0^S\,\psi^{S+} \;-\; G_c\Big(\frac{\phi^S}{\epsilon} - \epsilon \operatorname{div}\operatorname{grad}\phi^S\Big)\right]. \tag{8}$$

Since fracturing processes are irreversible in geomaterials, the restriction $(\phi^S)'_S \geq 0$ is included in terms of a history variable $\mathcal{H} = \max_{t>t_0}(\rho_0^S \psi^{S+})$ depending on the elastic-tensile energy $\rho_0^S \psi^{S+}$ according to [13].
As described in [10] and [12], a monolithic solution of the fully coupled set of governing equations for the biphasic TPM-phase-field model is numerically implemented in the in-house finite-element solver PANDAS.

3 Consideration of heterogeneities

Natural porous materials exhibit heterogeneities. Therefore, the inclusion of location-dependent material parameters is derived in this chapter. In contrast to stochastic phase-field modelling approaches, e. g. [16], a deterministic ansatz is investigated. Thereby, predefined imperfection areas are considered in Section 3.1 as well as statistical fields of geomechanical properties in Section 3.2. The main focus in this contribution is to discuss the impact of heterogeneities in porous media on the crack evolution and the crack path.

3.1 Consideration of material imperfection domains

Proceeding from the biphasic TPM-phase-field model introduced in Section 2, a numerical example with a homogeneous domain is compared with a two-zone model, containing a predefined (rectangular) imperfection area which is stiffer than the rest of the domain. Figure 1 (left) shows the basic two-dimensional initial-boundary-value problem (IBVP). The considered

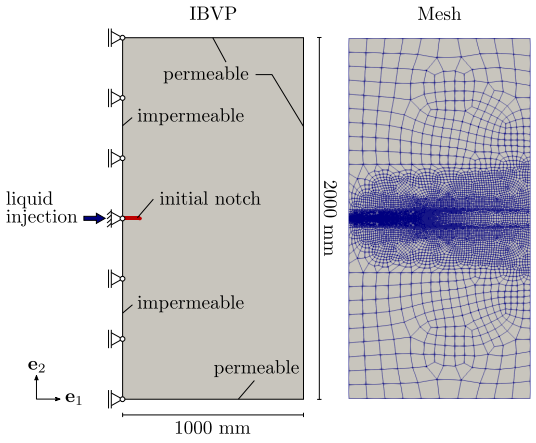

Fig. 1: Sketch of the initial-boundary-value problem (left) and finite-element discretisation (mesh) (right).

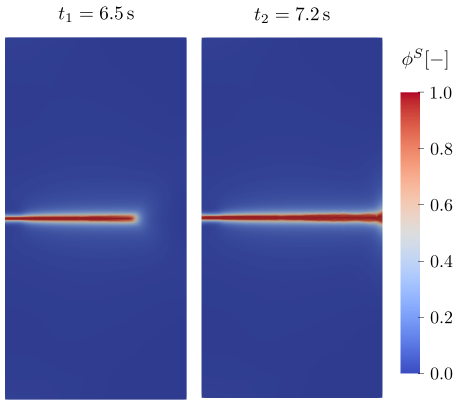

Fig. 2: Crack propagation in the homogeneous model at time $t_1 = 6.5\,\mathrm{s}$ and $t_2 = 7.2\,\mathrm{s}$.

domain of 1 m in length and 2 m in height is impermeable on its left and permeable on all the other edges. In the middle of the left edge, an initial notch of 100 mm length and 10 mm height is imposed via the initial pseudo-elastic energy (compare [12]). A liquid flow is injected with an increasing flow rate of $\bar{v}^L = 5 \cdot 10^{-3}\,t\,\mathrm{m}^3/(\mathrm{m}^2\mathrm{s})$, where t is the current time. The model is mechanically fixed at the left edge of the initial notch and constrained in normal direction on the whole left edge. The other three edges, the bottom, the right and the top, are free to move. Thereby, the boundary conditions induce a symmetric system in the $\mathbf{e}_2$-direction (gravitational forces are neglected). Note that no external forces are imposed on the system to avoid an influence on the crack propagation despite the local heterogeneity of the material properties. Table 1 lists the chosen material parameters, following [10, 11, 18]. Regarding the spatial discretisation of the model, a symmetric mesh with 8180 two-dimensional elements is chosen with a refined central area of the domain, see Figure 1 (right).

In the case of a homogeneous model with constant material parameters in the whole area, i. e. using the Lamé constants from Table 1, the crack evolves horizontally through the model until reaching the right edge at time $t_2 = 7.2\,\mathrm{s}$. Figure 2 shows the evolution of the phase-field variable after $t_1 = 6.5\,\mathrm{s}$ and $t_2 = 7.2\,\mathrm{s}$ for the homogeneous model.

In a next step, a rectangular area of 600 mm x 100 mm is predefined in front of the initial notch to model a two-zone domain. There, the Lamé constant λ^S is prescribed as ten times higher than in the rest of the model, see Figure 3. Note that

Table 1: Material parameters.

Parameter	Symbol	Value	Parameter	Symbol	Value
Lamé constants	μ^S	$8.077 \cdot 10^{10}\,\mathrm{Pa}$	Effective densities	ρ^{SR}	$3000\,\mathrm{kg/m^3}$
	$\lambda^S_{\mathrm{homogen}}$	$1.211 \cdot 10^{11}\,\mathrm{Pa}$		ρ^{LR}	$1000\,\mathrm{kg/m^3}$
Fluid viscosity	μ^{LR}	$10^{-3}\,\mathrm{Ns/m^2}$	Crack resistance	G_c	$2700\,\mathrm{N/m}$
Initial intrinsic permeability	K^S_{0S}	$1.0 \cdot 10^{-14}\,\mathrm{m^2}$	Length-scale parameter (crack)	ϵ	$0.01\,\mathrm{m}$
Initial porosity	n^F_{0S}	$0.20\,[-]$	Residual stiffness (crack)	η^S	$0.001\,[-]$

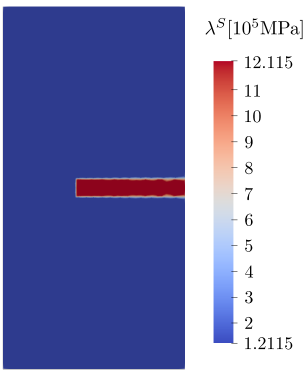

Fig. 3: Distribution of the Lamé constant λ^S in the idealised heterogeneous (two-zone) model.

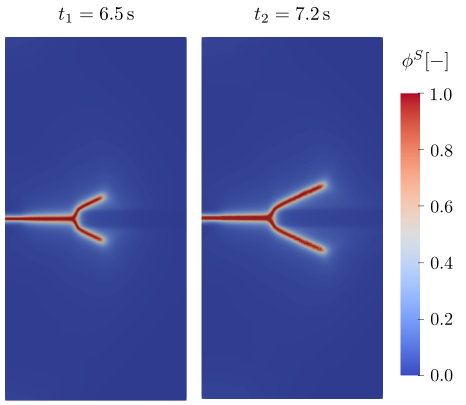

Fig. 4: Crack propagation in the idealised heterogeneous (two-zone) model at time $t_1 = 6.5\,\mathrm{s}$ and $t_2 = 7.2\,\mathrm{s}$.

the transition between the two areas is rather sharp. Such a material composition can be motivated, e. g., by layered rocks. As can be seen in Figure 4, the crack split into two branches in order to circumvent the stiffer area. Moreover, the crack branches reach the right edge later than in the homogeneous model, compare Figure 2 and Figure 4. Once the stiffer area is bypassed, the crack straightens towards the permeable edge. Thereby, the system is still symmetric due to the choice of the ideal (symmetric) problem. Note that the computation is carried out in a dynamic setting to enable a Navier-Stokes flow in the fully broken material, see Equation (5). However, caused by the local heterogeneity of the ideal material inclusion, the crack would split even in a fully quasi-static setting.

3.2 Statistical fields of geomechanical properties

In this subsection, a further generalisation of predefined zones of material imperfections, discussed in the previous section, towards a statistical distribution of geomechanical parameters is carried out. To start with, a normal distribution with possible enhancement towards more complex distributions is used. Since the statistical fields of the solid properties induce spatially varying local stresses, an influence on the crack path is expected.

3.2.1 Statistical definition of the parameter

To generate random realisations of material parameters, a Gaussian variogram is assumed [15]. According to Section 3.1, the focus is here on a statistical distribution of the Lamé constant λ^S. In this regard, the distribution of λ^S satisfies the following Gaussian variogram

$$p_{\mathrm{G}}(\lambda^S) = (2\pi)^{\frac{N_v}{2}} |\boldsymbol{\Sigma}|^{\frac{1}{2}} \exp\left(\tfrac{1}{2}\boldsymbol{\mu}^T \boldsymbol{\Sigma}^{-1} \boldsymbol{\mu}\right) \quad \text{with} \quad \Sigma_{ij} = \sigma^2 \left(1 - \exp\{-(|\,\mathbf{x}_i - \mathbf{x}_j|/\ell)^2\}\right) . \tag{9}$$

Thereby, $\boldsymbol{\mu}$ contains at each entry the mean value μ of the field, N_v represents the number of discretisation points, and $\boldsymbol{\Sigma}$ stands for the covariance matrix with coefficients Σ_{ij}. Moreover, σ^2 signifies the variance of the field, $\mathbf{x}_i$ and $\mathbf{x}_j$ are the vectors describing the positions of discretisation points, and ℓ is the so-called statistical length-scale parameter. This latter determines the spatial variance of the material parameter. Therefore, the smaller ℓ is chosen, the more significant the variance of λ^S to the next point, whereas, conversely, the larger ℓ is chosen, the smaller the change to the next point, see Figure 7. In particular, the parameters shown in Table 2 are used in this work. The corresponding normal distribution, which is fulfilled at each material point, is depicted in Figure 5. The generation of random material parameter fields is implemented on a regular grid using MATLAB.

Table 2: Statistical parameters.

Parameter	Symbol	Value
Mean value	μ	$5.05 \cdot 10^{11}$ Pa
Standard derivation	σ	$1.65 \cdot 10^{11}$ Pa
Statistical length-scale parameter	ℓ	$7, 70, 700$ mm
Number of discretisation points	N_v	120

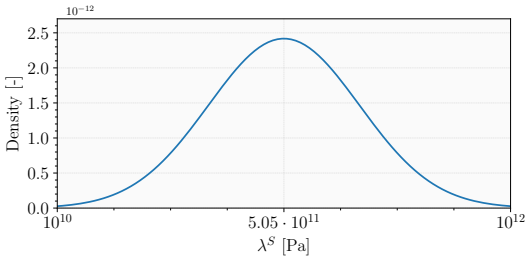

Fig. 5: Density curve of the Lamé constant λ^S.

3.2.2 Assignment of spatially-dependent material parameters

A customised algorithm is used for the assignment of the arbitrary heterogeneous parameter fields from Subsection 3.2.1 onto the meshing grid. In general, the spatial discretisation of the meshing grid is independent from material parameter data, given here in a regular distribution (Figure 6). It is often sufficient that each integration point K_G is basically equipped with the spatially closest material parameter data for a suitable spatial fit (Figure 6, green circle). However, a mismatch of integration points (Figure 6, red circle) combined with (sparse) data can cause inaccurate results. In this regard, a customised algorithm [17] is implemented and provides a suitable averaging process to allocate and store the material parameter information at each integration point K_G in a preceding calculation step for the subsequent numerical simulation.

Thereby, a (scalar-valued) material parameter μ^{K_G} is linearly weighted at the considered integration point K_G, viz.:

$$\mu^{K_G} = \frac{\sum_{\mathrm{n}} \mu^{\mathrm{data,n}}\, w^{\mathrm{data,n}}}{\sum_{\mathrm{n}} w^{\mathrm{data,n}}} \tag{10}$$

with $w^{\mathrm{data,n}} = 1 - d^{\mathrm{data,n}}/R_{K_G}$. Therein, $d^{\mathrm{data,n}}$ is the spatial distance of the material parameter data to the considered K_G within a certain (influence) radius R_{K_G} for K_G, see Figure 6. The superscript n is used to label the included material data points. The considered surrounding of K_G can either be chosen constant for the overall domain or location-dependent on the individual element size (via the Jacobian determinant $\bar{J}$ of the reference element).

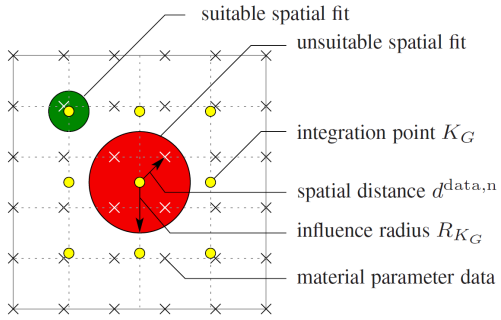

Fig. 6: Two-dimensional example of material-parameter assignment onto the integration points.

3.2.3 Numerical examples

In order to study the influence of statistical fields of geomechanical properties, the IBVP of Section 3.1 is now studied for different random distributions of the Lamé constant λ^S. The geostatistical fields are considered in terms of the definition and implementation described in Subsection 3.2.1 and Subsection 3.2.2. The mean value, which is chosen five times higher than the Lamé constant from Table 1, and the standard derivation are the same for all of the following examples, see Table 2. Only the statistical length scale parameter is varied, namely to 7 mm (Model 1), 70 mm (Model 2) and 700 mm (Model 3). This choice results in different structures of the Lamé-constant variations with the same (global) statistic distribution, see Figure 7. Each structure of the sample can be related to the microstructure of a specific porous material, e. g. with many smaller (Model 1) or a few larger (Model 3) areas with higher or lower stiffness. For all of the models, the influence radius R_{K_G} is set dependent on the individual element size, compare Subsection 3.2.2. Therefore, the smearing of the λ^S-variation in the upper and lower parts of Model 1 is due to the coarser mesh in these areas, see Figure 1 (right).

Figure 8 shows the crack evolution for each model at an intermediate time $t_1 = 6.5$ s and the final time $\bar{t}_2 = 8.0$ s, where the crack reaches the right edge for the three models. In Model 1, the statistical length scale parameter ℓ is chosen small, thus, the heterogeneities are in the order of a few elements. Physically, the crack follows always the path with the lowest resistance. Therefore, the crack evolves not straight horizontally to the right edge, as in the homogeneous model (compare Figure 2), but is interfered by the material parameter variations and shows a lot of fluctuations. Since the variations in the properties are very local in this model, the disturbed crack path is compensated such that the crack as a whole hits the right edge more or less in the centre. The most significant deflection of the crack path is visible in Model 2. Here, the statistical length scale parameter is chosen to be moderate such that the inclusions are in the order of magnitude of the initial notch length. As a result, the crack bypasses the areas of greater stiffness and winds around these inclusions, creating a wave-like crack field, see Figure 8. Finally, the statistical length scale parameter is set to 700 mm in Model 3, corresponding to the half domain width. Thereby, the heterogeneous inclusions are large in comparison to the notch dimensions. Here, the crack evolves more or less horizontally, as in the case of the homogeneous model, even that there is a considerable area of higher stiffness in front

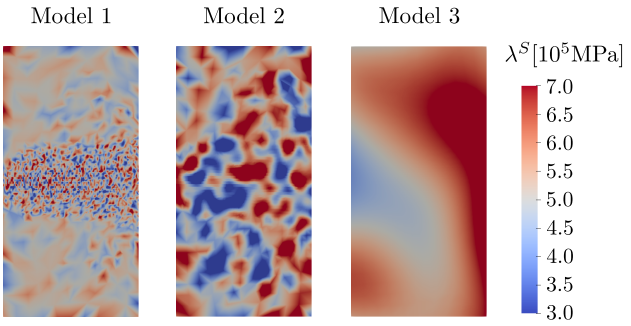

Fig. 7: Distribution of the Lamé constant λ^S for three different heterogeneous models using Gaussian variogram.

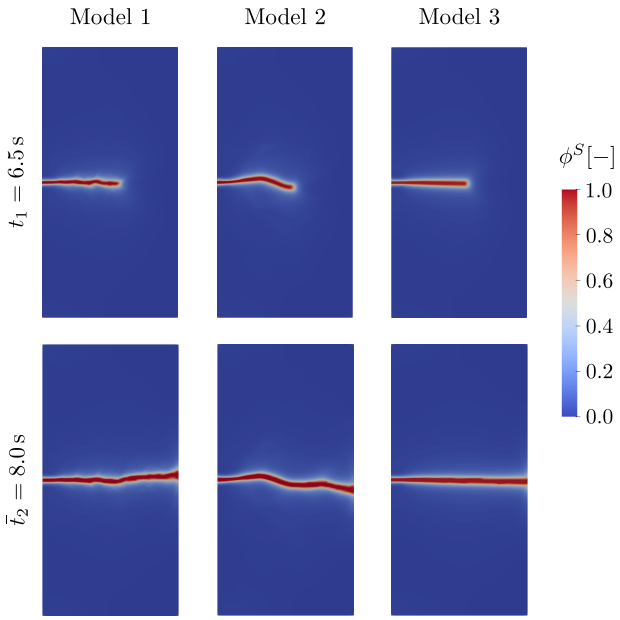

Fig. 8: Crack propagation for three different heterogeneous models at time $t_1 = 6.5\,\text{s}$ and $\bar{t}_2 = 8.0\,\text{s}$.

of the crack, similar to the idealised two-zone model from Section 3.1. This different behaviour is caused by the transition characteristics from softer to stiffer areas. In the two-zone model in Section 3.1, the transition is rather sharp, causing even a crack branching, see Figure 4. In contrast, the transition in Model 3 is rather smooth, compare Figure 7, and the crack tip does not notice a significant stiffness change. As a result, the crack slows down but stays on its original path and does not strike in a different direction.

To summarise the results, an affect on the crack evolution is clearly identified in models with small and moderate length-scale parameter, caused by the local variations of elastic stiffness properties representing a heterogeneous porous solid skeleton.

Acknowledgements Funded by the Deutsche Forschungsgemeinschaft (DFG, German Research Foundation) – Project Number 327154368 – SFB 1313. Open access funding enabled and organized by Project DEAL.

References

[1] M. A. Biot, J. Appl. Phys. **12**, 155–164 (1941).
[2] O. Coussy, Poromechanics (John Wiley & Sons, 2004).
[3] H. Steeb and J. Renner, Transp. Porous Med. **130**, 437–461 (2019).
[4] R. Helmig, Multiphase Flow and Transport Processes in the Subsurface (Springer-Verlag, Berlin, 1997).
[5] W. Ehlers and A. Wagner, Arch. Appl. Mech. **89**, 609–628 (2019).
[6] T. Cajuhi, L. Sanavia, and L. De Lorenzis, Comput. Mech. **61**, 299–318 (2018).
[7] C. Miehe and S. Mauthe, Comput. Methods Appl. Mech. Eng. **304**, 619–655 (2016).
[8] A. Mikelić, M. F. Wheeler and T. Wick, Multiscale Model. & Simul. **13**, 367–398 (2015).
[9] B. Markert and Y. Heider, in: Recent Trends in Computational Engineering-CE2014 (Springer, 2015), pp. 167–180.
[10] W. Ehlers and C. Luo, Comput. Methods Appl. Mech. Eng. **315**, 348–368 (2017).
[11] W. Ehlers, A. Sonntag and A. Wagner, in: Current Trends and Open Problems in Computational Mechanics (Springer, Cham, 2022), pp. 111–119.
[12] W. Ehlers and C. Luo, Comput. Methods Appl. Mech. Eng. **341**, 429–442 (2018).
[13] C. Miehe, M. Hofacker and F. Welschinger, Comput. Methods Appl. Mech. Eng. **199**, 2765–2778 (2010).
[14] C. Kuhn and R. Müller, Eng. Fract. Mech., **77**, 3625–3634 (2010).
[15] P. Kitanidis, Introduction to Geostatistics: Applications in Hydrogeology (Cambridge University Press, Cambridge, 1997).
[16] T. Gerasimov, U. Römer, J. Vondřejc, H. G. Matthies and L. De Lorenzis, Comput. Methods Appl. Mech. Eng. **372**, 113353 (2020).
[17] A. Wagner, Extended modelling of the multiphasic human brain tissue with application to drug-infusion processes (Dissertation, Stuttgart, 2014).
[18] U. Pillai,Y. Heider, and B. Markert, Computational Materials Science **153**, 36–47 (2018).

